Showcasing research from Professor Kirill Kovnir's group, Department of Chemistry, Iowa State University and US DOE Ames laboratory, Ames, Iowa, United States.

Synthesis-enabled exploration of chiral and polar multivalent quaternary sulfides

Highlighting an alternate synthetic pathway of formation of the members of the chiral and polar $La_6(TM)_xSi_2S_{14}$ (*TM* = transition metal) family of compounds by atomic mixing of the refractory reactants (metals and tetrels) through arc-melting and later reacting this mixture with sulfur.

Cover illustration by Grant Luhmann, Ames laboratory, US DOE.

As featured in:

See Kirill Kovnir *et al.*, *Chem. Sci.*, 2021, **12**, 14718.

ROYAL SOCIETY OF CHEMISTRY

rsc.li/chemical-science

Registered charity number: 207890

Chemical Science

ROYAL SOCIETY OF CHEMISTRY

EDGE ARTICLE

View Article Online
View Journal | View Issue

Cite this: *Chem. Sci.*, 2021, **12**, 14718

All publication charges for this article have been paid for by the Royal Society of Chemistry

Synthesis-enabled exploration of chiral and polar multivalent quaternary sulfides†

Georgiy Akopov, [ab] Nethmi W. Hewage, [b] Philip Yox, [ab] Gayatri Viswanathan, [ab] Shannon J. Lee, [ab] Liam P. Hulsebosch, [ac] Sarah D. Cady, [b] Alexander L. Paterson, [a] Frédéric A. Perras, [a] Wenqian Xu, [d] Kui Wu, [e] Yaroslav Mudryk [a] and Kirill Kovnir [*ab]

An innovative method of synthesis is reported for the large and diverse $(RE)_6(TM)_x(Tt)_2S_{14}$ (RE = rare-earth, TM = transition metals, Tt = Si, Ge, and Sn) family of compounds (~1000 members, ~325 contain Si), crystallizing in the noncentrosymmetric, chiral, and polar $P6_3$ space group. Traditional synthesis of such phases involves the annealing of elements or binary sulfides at elevated temperatures. The atomic mixing of refractory components technique, presented here, allows the synthesis of known members and vastly expands the family to nearly the entire transition metal block, including 3d, 4d, and 5d TMs with oxidation states ranging from 1+ to 4+. Arc-melting of the RE, TM, and tetrel elements of choice forms an atomically-mixed precursor, which readily reacts with sulfur providing bulk powders and large single crystals of the target quaternary sulfides. Detailed *in situ* and *ex situ* experiments show the mechanism of formation, which involves multiphase binary sulfide intermediates. Crystal structures and metal oxidation states were corroborated by a combination of single crystal X-ray diffraction, elemental analysis, EPR, NMR, and SQUID magnetometry. The potential of $La_6(TM)_x(Tt)_2S_{14}$ compounds for non-linear optical applications was also demonstrated.

Received 6th July 2021
Accepted 4th October 2021

DOI: 10.1039/d1sc03685h

rsc.li/chemical-science

Introduction

One of the main challenges of solid-state synthesis is the reactivity difference of the individual elements used as reactants.[1] This prevents or severely hinders the ability to form ternary and multinary compounds in single-phase form. Target complex multinary compounds are often accompanied by binary admixtures or become a minor product themselves, thus impeding property characterization. For example, synthesis using phosphorus prevents the direct melting of the target phase due to high vapor pressure of P. Moreover, annealing of elements with phosphorus often produces stable binaries, *e.g.*, AlP melting point is >2500 °C, which becomes the dead-end point of a synthesis. Using metallic or salt fluxes allows the synthesis of many complex phases, including those with volatile components, but flux reactions depend on the solubility of the reactants and might be compromised by an unintentional incorporation of flux elements into the products.[2–5]

One way of alleviating this problem is to use premixed reactants with similar reactivities that can be simultaneously introduced into the reaction mixture thus ensuring a full conversion to the product takes place. This can be achieved through the atomic mixing of components to achieve homogenous precursor reactants. We have demonstrated this approach for several ternary metal pnictides, where a metal–tetrel precursor (*e.g.*, LaSi) was made by arc-melting and reacted with a volatile pnictogen (P or As) at synthetic temperatures of 600–1050 °C, forming stoichiometric products such as: $LaSiP_3$,[6] La_2SiP_4,[7] AuSiAs,[8] $RuSi_4P_4$, and $IrSi_3P_3$.[9]

This precursor approach can be extended to more complex systems, combining several metals with vastly different melting points to produce single-phase products. One such complex system is a class of quaternary sulfides of type $(RE)_6(TM)_x(Tt)_2Q_{14}$ (RE = rare-earth metal; TM = transition metals; Tt = Si, Ge, and Sn; Q = S and Se) also referred as $(RE)_3(TM)_{x/2}(Tt)Q_7$. While in the present manuscript we focus

[a]*Ames Laboratory, U.S. Department of Energy, Ames, IA 50011, USA. E-mail: kovnir@iastate.edu*

[b]*Department of Chemistry, Iowa State University, Ames, IA 50011, USA*

[c]*Department of Physics, The State University of New York College at Buffalo, Buffalo, NY 14222, USA*

[d]*X-ray Science Division, Advanced Photon Source, Argonne National Laboratory, IL 60439, USA*

[e]*Hebei University, Baoding City, Hebei Province, 830011, China*

† Electronic supplementary information (ESI) available: Experimental details including synthesis descriptions as well as methods, figures, and tables pertinent to characterization techniques used: powder and single crystal X-ray diffraction, 17-BM *in situ* powder XRD, scanning electron microscopy, energy dispersive X-ray spectroscopy, electron paramagnetic resonance, nuclear magnetic resonance, DFT calculations, solid-state diffuse reflectance spectroscopy, magnetic measurements. Crystallographic data: CSD 2089782–2089797. For ESI and crystallographic data in CIF or other electronic format see DOI: 10.1039/d1sc03685h

only on transition metals, it should be noted that the role of the transition metal can be fulfilled by several main group metals, such as Li, Al, Sb, In, and Ga.[10–14]

$(RE)_6(TM)_xSi_2S_{14}$ ($x = 1$ and 2) phases for several rare-earth and transition metals were first mentioned in a 1969 paper by Michelet and Flahaut, where the authors used a reaction of binary sulfides at high temperatures (1350 °C).[15,16] The majority of later manuscripts focused on the crystal structures of Ge and Sn analogues with TM = Mn–Cu where syntheses from elements provide good yields of the target quaternary sulfides.[13,17–26]

All $(RE)_6(TM)_x(Tt)_2Q_{14}$ quaternary phases crystallize in the polar, chiral, noncentrosymmetric space group $P6_3$ (no. 173). With the ability of using rare-earth and transition metals, these phases have potential for interesting magnetic, non-linear optical, as well as piezoelectric properties. While several of the aforementioned papers analyzed the magnetic properties of selected $(RE)_6(TM)_x(Tt)_2Q_{14}$, many other papers explored the non-linear optical properties of similar compounds where the transition metal was replaced with Ga or Li: $La_6Ga(Ge/Ga)S_{14}$ (ref. 27) and $Sm_6Li_2Si_2S_{14}$.[28] The variety of all possible combinations of rare-earth and transition metals, tetrels (Si, Ge, and Sn), and chalcogenides (S and Se), gives rise to a remarkable number of almost 2000 quaternary phases (not counting solid-solutions), providing a broad avenue for property tuning and allowing computational explorations *via* machine-learning methods or high-throughput calculations. The exploration of Si analogues has been limited due to the difficulty of synthesis brought on by the relative inertness of Si, as compared to the other tetrels. Reported transition metals forming the $(RE)_6(TM)_xSi_2S_{14}$ phases were mainly limited to late 1st row (Mn–Cu) and Ag metals, significantly narrowing the potential phase space. In the current work we show that the $(RE)_6(TM)_xSi_2S_{14}$ system can be extended to include elements from almost the entire transition metal block with our developed synthesis method utilizing atomically mixed precursors. This method works for metals with a wide range of melting temperatures: from 1064 °C for Au to 2233 °C for Hf. It is important to reiterate that the reported here new compounds can be produced by other synthetic methods, such as reaction of elements or binary sulfides. Our control experiments show that the yield and selectivity of such reactions depends on the nature of the transition metal and require multiple regrindings and annealings. We are reporting the use of atomically-mixed precursors as a fast and facile alternative method to synthesize quaternary sulfides.

Using atomically mixed precursors not only allows to synthesize all the reported structures for TM^{2+} and TM^{1+} 1st row metals (Mn–Cu), but also enables the synthesis of new TM^{3+}- and TM^{4+}-containing $(RE)_6(TM)_xSi_2S_{14}$ and further expands the phase space to other 1st (Sc–Cr), 2nd (Zr, Ru–Ag), and 3rd (Hf, Ir–Au) row transition metals for silicon, germanium, and tin analogues.

Lowering of the reaction temperature to stabilize complex metastable or stable compounds is a common goal for solid state synthesis,[2–4,29–48] such as formation of metastable forms of RE oxychlorides *via* low-temperature pyrohydrolysis of $(NH_4)_3REC1_6$.[49] The mixing of the rare-earth and transition metals in the silicide precursors is somewhat akin to eutectic fluxes used in the Latturner group to make metal-rich intermetallics,[29–34] as well as flux syntheses of complex intermetallics performed by other groups.[2–4,35–48]

In situ powder X-ray diffraction study was used to elucidate the mechanism of formation of such quaternaries. Detailed structural characterization by single crystal X-ray diffraction and ^{29}Si and ^{45}Sc solid-state nuclear magnetic resonance (NMR) and electron paramagnetic resonance (EPR) spectroscopies are reported. Semiconducting nature of the produced materials was confirmed by UV-Vis diffuse reflectance spectroscopy, and selected examples of magnetic and non-linear optical properties are provided.

Experimental methods

A detailed description of synthetic, characterization, and analysis methods are provided in ESI.† Bulk powders of the different members of $La_6(TM)_x(Tt)_2S_{14}$ (Tt = Si, Ge, Sn; $x = 0.5$–2) were prepared using arc-melted metal–tetrel precursor and sulfur. The addition of a potassium iodide (KI) salt flux resulted in mm-long needle-like single crystals.

Synthesized phases were analyzed by laboratory powder and single crystal X-ray diffraction (PXRD and SCXRD), synchrotron *in situ* PXRD at the 17-BM beamline at the Advanced Photon Source at Argonne National Lab (APS ANL), ^{29}Si and ^{45}Sc solid-state NMR spectroscopy and EPR spectroscopy; optical bandgaps were measured using a UV/Vis diffuse-reflectance spectroscopy. Non-linear optical properties (second harmonic generation, SHG) were analyzed using a Q-switch laser setup through Kurtz and Perry method, while LDT was evaluated using a pulsed YAG laser. Magnetic properties were measured using a superconducting quantum interference device (SQUID) magnetometer, model MPMS XL-7, manufactured by Quantum Design.

Results and discussion

Crystal structure

The quaternary $La_6(TM)_x(Tt)_2S_{14}$ phases crystallize in the polar, chiral, noncentrosymmetric $P6_3$ space group, with the main difference between the phases being the relative amounts of transition metal in the structure (Fig. 1 and 2). The crystal structure is composed of $[LaS_7]$ prisms, $[(TM)_xS_6]$ octahedra, and $[SiS_4]$ tetrahedra. Face-sharing $[LaS_7]$ prisms form spiral columns, which wind around a channel of face-sharing $[(TM)_xS_6]$ octahedra. Each spiral column of $[LaS_7]$ units is surrounded by six $[SiS_4]$ units, also arranged in columns.

For $La_6(TM)_xSi_2S_{14}$ (Fig. 2), the metal content, x, depends on the metal oxidation state (n) and is equal to $2/n$, taking into account charge balance, $(La^{3+})_6(TM^{n+})_x(Si^{4+})_2(S^{2-})_{14}$. Thus, for monovalent metals Cu, Ag, and Au, $x = 2$, and such metals are located on the opposite trigonal faces of S_6 octahedra. For previously reported divalent Mn–Ni, $x = 1$, which was confirmed by our SCXRD experiments and elemental analyses. Such metals are located in the center of S_6 octahedra and have site

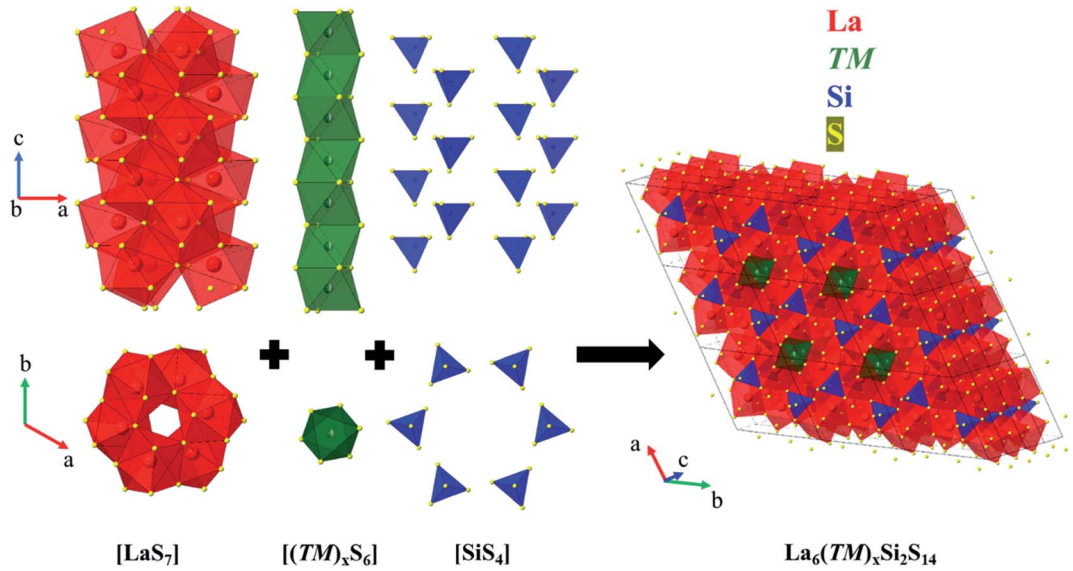

Fig. 1 Crystal structures of $La_6(TM)_xSi_2S_{14}$ ($x = 0.5–2$). The crystal structure is composed of face-sharing [LaS_7] polyhedra arranged in a spiral column (red), a chain of face-sharing S_6 octahedra (green) hosting transition metals and columns of [SiS_4] tetrahedra (blue). TM occupancy and position inside S_6 octahedra is dependent on the nature of the metal. In the case of 1+ transition metals (Cu, Ag, and Au), the metals are located not in the center but on shared trigonal faces of the S_6 octahedra.

occupancies of 50%, indicating that statistically half of the octahedra are vacant. For early 1st row metals (Sc, Ti, and Cr), as well as for Rh and Ir, $x = 0.67$, indicating a 3+ oxidation state. This oxidation state was reported for similar compounds with main group elements Al, Sb, and In,[10,11,14] but was not reported for transition metals. Finally, for Zr, Hf, and Pt, $x = 0.5$ and suggests a 4+ oxidation state. Both 3+ and 4+ metals are also located in the center of S_6 octahedra, but with only 1/3 or 1/4 of octahedra hosting a transition metal. The low site occupancy of transition metal results in split positions for S atoms, forming empty expanded and filled contracted $(TM)S_6$ octahedra. Fig. S1† shows the correlation between the unit cell parameters, volume, and ionic radii of the transition metal.

The structure of $La_6Au_2Si_2S_{14}$ is similar to that of the Cu analogue, where the [AuS_3] trigonal planar units occupy the faces of face-sharing octahedra. The Au–Au distance in this structure is 2.913 Å indicating the possibility for aurophilic interactions.[8,51,52] The Au–S distances are 2.424 Å, which is significantly longer than Au–S bonds in Au_2S – 2.17 Å.[53] In the majority of multinary sulfides, the Au–S distance is ~2.30 Å, but in some cases longer distances of 2.35–2.37 were reported.[54,55] Replacing monovalent Au with monovalent Li results in $La_6Li_2Si_2S_{14}$, where Li^+ occupies the centers of the octahedra (LiS_6) instead of on the faces (AuS_3), due to the size difference between Li and Au.[28,56]

For $La_6(TM)_xSi_2S_{14}$ (TM = Mn, Fe, Co, and Ni), the transition metal content is 50% of the 2-fold site, and [$(TM)S_6$] octahedra are almost regular with TM-S distances of 2.64–2.66 Å (Mn), 2.61–2.62 Å (Fe), 2.61–2.63 Å (Co), and 2.590–2.593 Å (Ni).

For $La_6(TM)_xSi_2S_{14}$ (TM = Sc, Ti, and Cr), the transition metal content is 33% of the 2-fold site. This partial occupancy leads to split S sites, where the empty S_6 octahedra are substantially

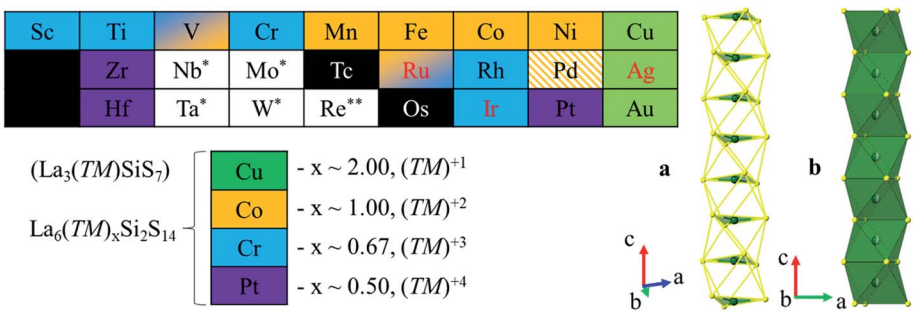

Fig. 2 Summary of transition metal oxidation states and occupancies for $La_6(TM)_xSi_2S_{14}$ (TM = most transition metals). Monovalent metals ($x = 2$) occupy the trigonal faces of the octahedra (a); for $x = 1–0.5$, the metals occupy the centers of the octahedra (b). For metals in red, we were unable to grow single crystals, therefore the oxidation state is attributed according to EDS data. For Ag literature data was used.[50] For metals with (*) bulk phase/single crystal growth failed for La–TM–Si–S composition, but there is indication of formation of the target quaternary phase with either other rare-earth metals or other tetrels. (**) For Re quaternary phase formation failed for all attempts with Si, Ge and Sn.

expanded by ~30% (Table S8†). The 3+ oxidation states for those metals were confirmed with EPR and NMR measurements (*vide infra*). Sc–S, Cr–S, and Ti–S interatomic distances in the quaternary sulfides (2.60–2.61 Å, 2.54–2.55 Å, and 2.56–2.57 Å, respectively) are longer than those in the corresponding binary sulfides (Table 1). However, similar long distances were reported for $U_2Ti^{III}S_5$.

$La_6V_{0.77}Si_2S_{14}$ is a special case, where the metal content is neither the expected $x = 0.67$ nor 1. This V content was reproduced in several SCXRD experiments, while EDS elemental analysis provides V content as 0.69(4) (Table S4†). For both V neighbors, Ti and Cr, the metal content from single crystal diffraction experiments and EDS were close to expected 0.67. This may suggest that V exhibits mixed oxidation states, but such hypothesis needs further spectroscopic verification. Unfortunately, we were not able resolve the vanadium ion signal in EPR down to 6 K. The V–S distances are 2.55 Å, consistent with V–S distances reported for polymorphs of V_4GeS_8 (Table 1).

$La_6Rh_{0.67}Si_2S_{14}$ is another example of the transition metal in 3+ oxidation state, which leads to a d^6 electron configuration, low-spin, as evident by solid state NMR experiments. The Rh–S distances in the quaternary phase, 2.53–2.54 Å, are longer than ones in Rh_2S_3 but comparable to the Rh–S distances in ternary Rh sulfides (Table 1).

For $La_6(TM)_xSi_2S_{14}$ (TM = Zr, Hf, and Pt), the transition metal content is 25%, meaning only a quarter of octahedra are occupied again leading to split S sites. The TM-S distances in the quaternaries are 2.62–2.64 Å (Zr and Hf) and 2.56–2.58 Å (Pt). These distances are longer than the corresponding metal–sulfur distances in $(TM)S_2$ sulfides and are comparable to distances in $(TM)S_3$ and some multinary sulfides (Table 1).

Pd appears to be another special case, the metal stays in the 2+ oxidation state, as implicated by the composition determined *via* both SCXRD refinement and EDS data (Table S4†). A substantial distortion of the octahedra occurs resulting in local square-planar coordination of Pd with two additional very distinct apical S atoms. This distortion causes the space group to change from hexagonal to monoclinic chiral and polar $P2_1$. The growth of high quality $La_6PdSi_2S_{14}$ crystals was not possible due to extensive twinning issues; a full structural refinement of this phase will be published elsewhere.

Table 1 Reported values of metal–sulfur bond lengths for select binary and ternary sulfides

Metal sulfide	d(M–S) (Å)	Ref.	Metal sulfide	d(M–S) (Å)	Ref.
Sc_2S_3	2.57–2.59	57	ZrSiS	2.65–2.83	58
$Ti^{IV}S_2$	2.42	59	Rh_2S_3	2.31–2.40	60
$Ti_2{}^{III}S_3$	2.41–2.48	61	BiRhS	2.45	62
$LiTiS_2$	2.48	63	Co_8RhS_8	2.50	64
$U_2Ti^{III}S_5$	2.61–2.85	65	HfS_2	2.55	66
V_4GeS_8 ($F\bar{4}3m$)	2.29–2.55	67	HfS_3	2.59–2.69	68
V_4GeS_8 ($Imm2$)	2.19–2.82	69	HfSiS	2.65–2.77	58
Cr_2S_3	2.37–2.44	70	PtS_2	2.34	71
ZrS_2	2.57	72	$PtCuAsS_2$	2.48–2.66	73
ZrS_3	2.60–2.72	68	Au_2S	2.17	53

For TM = Ru and Ir, we were unable to grow crystals suitable for SCXRD analysis. Oxidation state was assigned only based on the composition determined by EDS. Similarly, to V, the Ru analogue may be present in a mixed 2+/3+ oxidation state because the metal content is in between 0.67 and 1.0 (Table S4†). Lastly, for the Ir analogue, the transition metal seems to be in a 3+ state similar to Rh case. Low-spin d^6 electronic configuration of Ir was indirectly confirmed by SQUID magnetometry data showing the Ir analogue to be diamagnetic.

For the position inside the S_6 octahedron, the metal atom should be of an appropriate size. Metal radius mismatch might explain why it is challenging to make $La_6(TM)_xSi_2S_{14}$ with TM = Nb, Ta, Mo, W, or Re. Using a combination of Shannon's metal ionic radii for octahedral environments[74] and an estimation of the same radii using average TM-S bond distances and the ionic radius of S^{2-} (Table S8A†), we have come up with the metal ionic radius range, 0.63–0.83 Å, necessary to accommodate the (TM) S_6 octahedra for $La_6(TM)_xSi_2S_{14}$ analogues. Furthermore, using this range we can predict that the unexplored TM's should be accommodated in the structure as following (bolded most favorable case): Nb (3+, 4+ or **5+**), Mo (3+ or **4+**), Ta (3+, 4+ and **5+**), W (**4+** or 5+), Re (**4+**), and Os (**4+**) (Table S8B†). Our limited PXRD and EDS data suggest that these transition metals can be incorporated into the structure of $(RE)_6(TM)_xSi_2S_{14}$ for smaller rare-earth metals (RE = Gd and Tb).

Synthesis

Bulk powders of $(RE)_6(TM)_x(Tt)_2S_{14}$ (RE = Sc, Y and La, TM = groups 3–11 (excluding Tc and Os); Tt = Si, Ge, and Sn) were prepared using the pre-arc-melted rare-earth transition metal tetrelide precursor and appropriate stoichiometric quantities of sulfur without flux, with dwell times of 72–120 hours at a maximum dwell temperature of 900 °C to 1050 °C, depending on the transition metal and tetrel used. Table S2† lists all the precursors used and the phases present in the brittle fraction of each precursor. Tables S3A–C and Fig. S3A–E† contain the phase compositions for all reactions with La, Y, and Sc; different TMs; different tetrels (Si, Ge, and Sn); and S. Additionally, Te-containing samples were made to probe the possibility to form analogues quaternary phases with the heaviest stable chalcogen.

$(RE)_6(TM)_x(Tt)_2Q_{14}$ quaternary system is extensively studied for germanium–selenium analogues, because those phases for the most part can be synthesized from elements.[21,22,24,25,27,28,75] For Si-containing systems, the typical synthesis from elements at a temperature of ~1000 °C resulted in poor yield of the quaternary compounds as products are dominated by binary and ternary sulfides. Some quaternary phases have been synthesized using binary sulfides at elevated temperatures;[15] however, this synthesis is limited by the availability of binary metal sulfides.

Metal silicide precursors have two major advantages: (i) it is possible to achieve atomic mixing of the refractory constituents; and (ii) both the reactive metal and less reactive silicon are simultaneously introduced into the reaction mixture upon reaction of the precursor with sulfur at relatively low

temperatures. Both advantages are demonstrated in the *in situ* and *ex situ* PXRD (Fig. 3 and S2), which emphasizes the absence of unreacted Si species throughout the reaction.

In situ synchrotron PXRD experiments at 17-BM at APS were conducted to study formation of the $La_6Rh_{0.67}Si_2S_{14}$. The reaction capillary was loaded with an arc-melted "$La_6Rh_{0.7}Si_2$" precursor and sulfur in a 1 : 14 molar ratio. The precursor reacts shortly after sulfur has melted with the formation of lanthanum and silicon sulfides at temperatures lower than 200 °C (Fig. 3). As the temperature increases to above 540 °C, rhodium sulfide forms. Due to the initial mixing of metals and Si, we hypothesize that the formed binary sulfides are also properly mixed and not spatially segregated. At above 760 °C, three binary sulfides react to form the target quaternary metal sulfide. The sample remains unchanged on cooling with only excess sulfur precipitating back into a solid, which indicates that the phase formation happens upon heating of the reaction mixture.

Similar conclusions can be drawn when analyzing *ex situ* PXRD data for $La_6CoSi_2S_{14}$ sample (Fig. S2†) by reacting the precursor metal silicide and sulfur, then dwelling the mixture at variable temperatures. It should be noted that this method does not allow to determine whether intermediate phases form upon heating. Here we can again see the formation of binary sulfides upon the decomposition of the precursor and the formation of a quaternary phase at ~750 °C.

To test how synthesis using an arc-melted precursor compares to traditional synthesis from elements and binary sulfides, we performed control syntheses of quaternary phases with TM = Ti and Rh. Using the same reaction temperature and duration, syntheses were performed starting from either the mixtures of elements or mixture of pre-synthesized binary sulfides. In the case of TM = Ti, both control syntheses resulted in the formation of the target quaternary phase with different amounts of admixtures (Fig. S3F†). However, in the case of TM = Rh, both syntheses resulted in non-homogeneous samples where the target quaternary phase was only a minor byproduct. Multiple regrindings and annealings might be required to form the target quaternary phases in high yields when starting from elements or binary sulfides.

Fig. 4 shows several representative PXRD patterns for the quaternaries for Co, Rh, Ir, Cu, Ag, and Au. Changing the precursor composition from $La_6(TM)Si_2$ to $La_6(TM)_{0.67}Si_2$ for TM = Rh and Ir resulted in the elimination of binary transition metal sulfides from the products, thus confirming the corresponding occupancy of the transition metal. Using this method, we were able to reproduce the reported quaternary phases with Mn, Fe, Co, Ni, Cu, and Ag. Moreover, we were able to expand this family of compounds to other 1st (Sc, Ti, V, and Cr), 2nd (Zr, Ru, Rh, and Pd) and 3rd (Hf, Ir, Pt, and Au) row transition metals (Table S3A and Fig. S3A–E†). For certain cases, the precursors with Ge or Sn (*e.g.*, $La_6MnGe_2S_{14}$ and $La_6MnSn_2S_{14}$) resulted in the formation of cleaner samples than in the case of Si, presumably due to the increased brittleness of the precursors (Table S2†) which ensures better mixing of the precursor with S. In other cases, quaternaries with Ge or Sn failed to form, which could be explained by the elevated maximum dwell temperature used and could be alleviated by synthesis at lower temperatures. A notable exception is Re, which failed to be incorporated into the quaternary structure for all 3 tetrel cases: Si, Ge, and Sn (Table S3A and Fig. S3B†).

For La–Ge–S and La–Sn–S, there exist ternary phases ($La_6Tt_{2.5}S_{14}$)[76] crystallizing in the same space group $P6_3$. Thus, La–TM–{Ge,Sn}–S quaternary compounds require elemental analysis to confirm the presence of the transition metal. On the other hand, for La–Si–S, the ternary phase La_2SiS_5 (ref. 76) crystallizes in a different crystal structure with the $P2_1/c$ space group and has a distinctly different PXRD pattern, showing further proof of target quaternary phase formation (Fig. 5).

The synthetic method reported here has an important limitation – the increased ductility of the arc-melted precursor. The precursor is not a single compound but a mixture of La and transition metal silicides and, in some cases, elemental transition metal. Phase segregation and formation of non-brittle phases prevent obtaining a powdered precursor with the

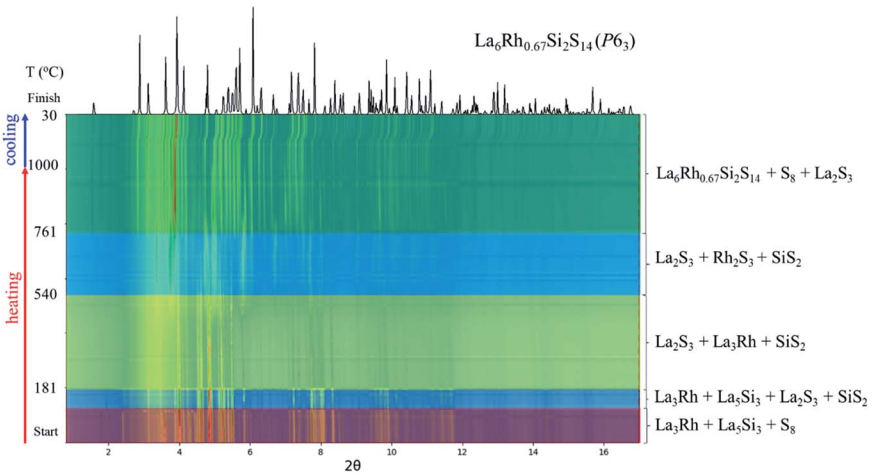

Fig. 3 *In situ* PXRD patterns showing $La_6Rh_{0.67}Si_2S_{14}$ phase formation collected at the 17-BM beamline at Argonne National Lab. The pre-arc-melted "$La_6Rh_{0.7}Si_2$" and S reactants form $La_6Rh_{0.67}Si_2S_{14}$ ($P6_3$) at ~760 °C. Synchrotron X-ray wavelength λ = 0.24145 Å.

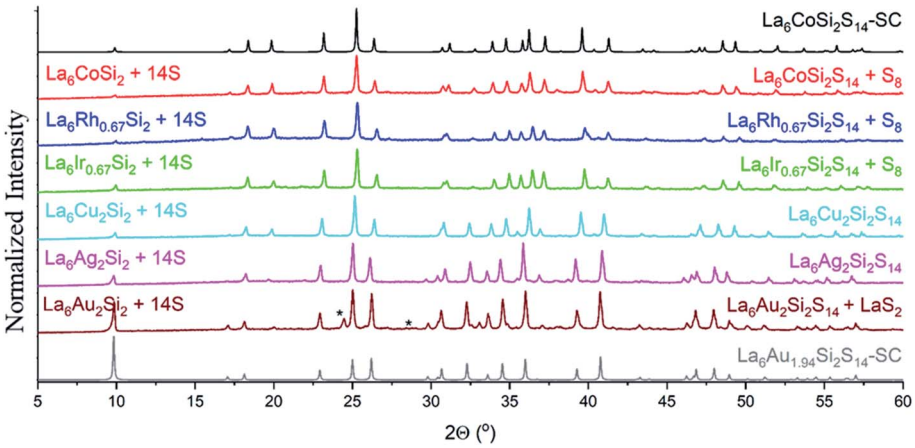

Fig. 4 PXRD patterns showing phase formation for $La_6(TM)_xSi_2S_{14}$ (TM = Co, Rh, Ir, Cu, Ag, and Au). Precursors for Rh and Ir were optimized to contain $x = 0.67$ equivalents of the transition metal, which produce single-phase samples. Top and bottom patterns in black and grey (Co and Au) are calculated from SCXRD structures. Peaks corresponding to LaS_2 secondary phase are indicated by (*).

desired stoichiometry. In the cases of TM = V, Zr, Nb, Mo, Hf, and Ta, a reaction of the pre-arc-melted $La_6TM_xSi_2$ with sulfur resulted in the formation of a mixture of La_2SiS_5 ($P2_1/c$) ternary compound and binary sulfides. This is mainly pronounced for La and could be alleviated by using a different lanthanide, Ce–Er (except for Pm and Eu). Another way to overcome this limitation is to arc-melt two separate binary silicides of La and TM, and then mix them together. This ensures the brittle nature of the precursors, which can facilitate further reaction. Thus, synthesis using a mixture of La_5Si_3 and TM–Si precursors resulted in the formation of the $La_6(TM)_xSi_2S_{14}$ quaternary phase for TM = V, Zr, and Hf. Fig. 5 shows the formation of the $La_6V_{0.7}Si_2S_{14}$ phase from La_5Si_3 and V_5Si_3 precursors. Using "La_6VSi_2" as a precursor resulted in the formation of a majority La_2SiS_5 phase. The successful formation of quaternary targets from binary silicides indicated that the mixing of metals and Si is more important than the mixing of transition and rare-earth metals. It should be noted that using a mixture of individual metal silicide precursors results in a non-stoichiometric amount of silicon and cannot be used to make single phase bulk powders, however, it is suitable to grow large single crystals of such compositions.

In order to grow single crystals of the reported and novel $La_6(TM)_xSi_2S_{14}$ compounds, potassium iodide (KI) flux.[5,53,54] was used in a 1 : 30 mass ratio for (precursor + sulfur) to KI using a similar temperature profile as for bulk powder synthesis. Depending on the transition metal and tetrel, different sizes of crystals were observed, ranging from thin hexagonal needles (1–3 mm in length) to bulky short hexagonal rods ($\sim 1 \times 1$ mm^2 in cross section) (Fig. 6 and S7†).

Yttrium and scandium were probed for their ability to form quaternary phases targeting $Y_6(TM)_xSi_2S_{14}$ and $Sc_6(TM)_xSi_2S_{14}$

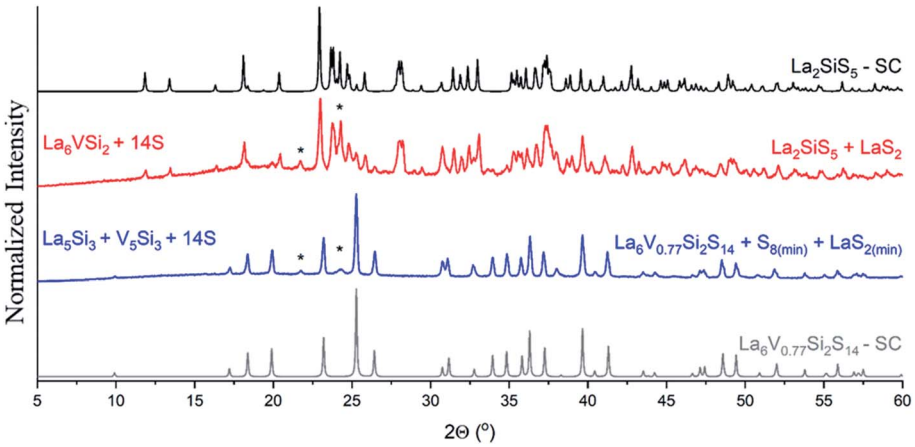

Fig. 5 PXRD patterns showing phase formation for $La_6V_{0.7}Si_2S_{14}$: red pattern corresponds to products of the reaction of the arc-melted "La_6VSi_2" precursor and S, while blue pattern corresponds to products of reaction of La_5Si_3, V_5Si_3, and sulfur. Both reactions were run at the same temperature profile in the same furnace. Using a ternary precursor in this case resulted in the formation of majority ternary sulfide, La_2SiS_5 ($P2_1/c$),[76] while using two binary precursors resulted in the formation of a target hexagonal ($P6_3$) quaternary structure. Patterns in black (ICSD 240952 (ref. 19)) and grey are calculated from single crystal structural data. Peaks corresponding to LaS_2 secondary phase are indicated by (*).

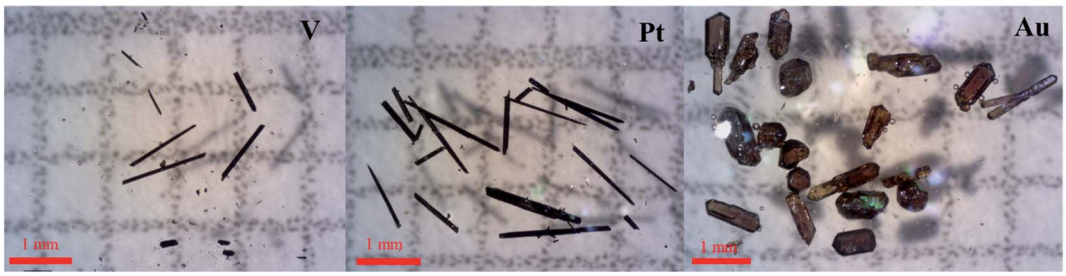

Fig. 6 Optical images of select crystals for $La_6(TM)_xSi_2S_{14}$ (TM = V (left), Pt (middle), and Au (right)). Each cell on the graph paper is 1 × 1 mm.

compositions using the precursor synthesis (Table S3B and Fig. S3E†). We were able to form several target quaternary phases with yttrium, however, the same synthetic conditions with scandium did not yield any quaternary phases, with most of the products being binary sulfides. Scandium is a metal which can act in both transition and rare-earth metal roles.[77] For example, in metal borides, scandium can both form AlB_2- and UB_{12}-type structures, ScB_2 and ScB_{12},[78] acting as a transition metal, as well as $ScCrB_4$ and Sc_2ReB_6,[79] acting as a rare-earth metal. Probing this hypothesis, it was found that indeed Sc acts as a 3+ transition metal in this case and we successfully synthesized $La_6Sc_{0.67}Si_2S_{14}$ and $La_6Sc_{0.67}Ge_2S_{14}$.

Selenium analogues of the target quaternary phases are heavily studied in literature,[17,18,23,27,28,75,80] and we attempted to explore whether tellurium can form similar phases. Unfortunately, in all cases using the same precursors and tellurium resulted in the formation of binary or ternary tellurides at various synthetic temperatures (750, 900 and 1050 °C) (Table S3C†).

SEM/EDS. Energy dispersive X-ray spectroscopy (EDS) was used to validate the transition metal content for the quaternary phases. Backscattered electron images for some of the crystals of the quaternary compositions can be seen in Fig. S6,† showing the predominant morphology of hexagonal rods. The EDS results are summarized in Table S4† and are in good agreement with the SCXRD determined compositions (Table S1†).

^{29}Si and ^{45}Sc solid state NMR. Of the elements incorporated in these ternary phases, ^{29}Si and ^{45}Sc have the most favorable NMR properties and enable the study of the silicon and transition metal sites in the diamagnetic quaternary phases. In particular, NMR should enable the detection of potential amorphous phases or byproducts that are difficult to observe *via* X-ray diffraction, as well as reveal any positional disorder that may have been missed in the crystal structure refinement. Such potential disorder includes either Si mixing with TM in the octahedral site, as was reported for other lanthanides $RE_6(Si^{tetr})_2(Si^{oct})_{0.5}S_{14}$;[81] or partial mixing of Sc with La.

We were able to detect the ^{29}Si NMR resonance in $La_6Cu_2Si_2S_{14}$, $La_6Ag_2Si_2S_{14}$, $La_6Au_2Si_2S_{14}$, $La_6RhSi_2S_{14}$, and $La_6Sc_{0.67}Si_2S_{14}$ with the use of low-temperature (100 K) magic angle spinning (MAS) for sensitivity enhancement. We were unsuccessful in detecting the ^{29}Si resonance in $La_6Ti_{0.67}Si_2S_{14}$ and $La_6Ir_{0.67}Si_2S_{14}$, presumably due to either long longitudinal relaxation times, broad linewidths, or the paramagnetic nature of Ti-containing compound. Our attempts to apply pulse cooling dynamic nuclear polarization (DNP) to increase sensitivity were unsuccessful, perhaps due to the lower spin density in these materials when compared to prior literature reports.[82] All ^{29}Si chemical shifts fall in a narrow range from 0.4 to 7.7 ppm, in agreement with those of SiS_4 tetrahedra,[83] and were sensitive to the identity of the transition metal, despite its remote location relative to the silicon. In the $La_6(TM)_2Si_2S_{14}$ series, where TM = Cu, Ag, Au, a steady increase in the ^{29}Si chemical shift was observed with the increasing atomic number of the metal. The increase could be reproduced using gauge-including projector-augmented-wave (GIPAW)[84,85] density-functional theory (DFT) calculations, however the increase was slightly overestimated. This difference may be caused by a lack of spin–orbit relativistic effects in the calculations, which are expected to be important in the case of Au.[86] The experimental and DFT-calculated ^{29}Si chemical shifts are listed in Table S5† and the spectra are depicted in Fig. 7b. In all cases only a single resonance was observed indicating that there is little, if any, positional disorder at Si in the studied materials, *i.e.* no TM/Si mixing.

^{45}Sc MAS NMR spectra were acquired for the $La_6Sc_{0.67}Si_2S_{14}$ and $La_6Sc_{0.67}Ge_2S_{14}$ compounds and are depicted in Fig. 7a. In both materials a sharp resonance was observed for the quaternary phase along with the signal from a $LaScS_3$ impurity. Importantly, the fact that only a single site was observed confirms that Sc does not occupy the rare-earth metal site of the crystal structure. The electric field gradient (EFG) tensor parameter at the Sc center could not be determined using lineshape analysis, however we were able to apply the two-dimensional one-pulse (TOP) method[87] to separate the signals from the central transition ($m = 1/2$ to $-1/2$) and inner satellite transitions ($m = 3/2$ to $1/2$ and $-1/2$ to $-3/2$) and determine the isotropic chemical shifts and quadrupolar products (P_Q) of the ^{45}Sc sites through the transitions' differing second-order quadrupole shifts (more details are given in the ESI†). Those parameters are tabulated in Table S6.† The obtained EFG tensor parameters were in good agreement with those predicted using the GIPAW DFT calculations. There were no large differences in either the ^{45}Sc chemical shift or P_Q values measured for $La_6Sc_{0.67}Si_2S_{14}$ and $La_6Sc_{0.67}Ge_2S_{14}$, again likely due to the remote position of the tetrel relative to the transition metal site.

EPR. Electron paramagnetic resonance (EPR) analysis was performed on select $La_6(TM)_xSi_2S_{14}$ (TM = Ti, V, and Cr) to confirm the oxidation state of the transition metal (Fig. S8†).

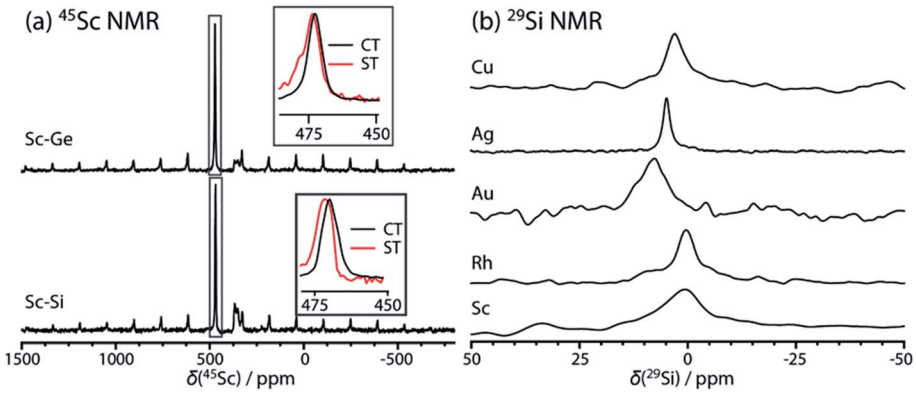

Fig. 7 ^{45}Sc (a) and ^{29}Si (b) MAS NMR spectra of $La_6(TM)_xSi_2S_{14}$ and $La_6Sc_{0.67}Ge_2S_{14}$ with metals indicated on the figure next to each spectrum. In (a), insets are used to show the centerbands of the central transition (CT, black) and inner satellite transition (ST, red).

EPR data showed the metal ions to be Ti^{3+} and Cr^{3+} with g values of 2.01246 and 1.99336,[88,89] respectively, which is in good agreement with SCXRD (Table S1A†) and EDS data (Table S4†). This further shows that Ti has 3+ oxidation states while its neighbors in group 4 (Zr and Hf) have 4+ oxidation states (Tables S1B and S4†). In the case of V, the EPR spectrum at 6 K did not have adequate signal-to-noise ratio for a proper assignment.[90,91]

Optical properties. All the studied quaternary phases are colored semiconductors with band gaps of 1.5–2.6 eV (Ti–Au) as analyzed by diffuse reflectance UV-vis spectroscopy (Fig. S4 and S5†). Furthermore, since all these quaternaries crystallize in the polar, chiral, noncentrosymmetric $P6_3$ space group, they are good candidates for second-harmonic generation (SHG).[92–94] We performed preliminary tests for group 9 and 11 metal–Si compounds (Fig. 8 and Table S7†) which show that the SHG response depends on the nature of the transition metal indicating promise of this large group of nearly 2000 transition metal compounds for non-linear applications. We have also measured the laser-damage thresholds (LDTs) of the title compounds, generally increasing with the size of a material's band gap. For phases with Si, the results show that $La_6Cu_2Si_2S_{14}$ exhibits the highest LDT from the set, which is about 5.0 times that of $AgGaS_2$. The other quaternary phases exhibit comparative LDTs with that of $AgGaS_2$ (Fig. 8). Quaternary Rh and Ir sulfides have SHG signals comparable to that for the $AgGaS_2$ standard at smallest measured particle size. While majority of $La_6(TM)_xSi_2S_{14}$ phases studied here show no phase matching, $La_6Cu_2Ge_2S_{14}$ exhibits not only phase matchability but also SHG values comparable to the $AgGaS_2$ standard (Table S7†). The obtained non-linear optical properties are comparable to other TM-free studied analogues in this family, $\times$0.5–1.8 SHG and $\times$2.5–6 LDT as compared to those for $AgGaS_2$: $La_6Li_2Ge_2S_{14}$, $La_6Li_2Sn_2S_{14}$,[56] $Sm_6Li_2Si_2S_{14}$,[28] $La_6Sb_{0.66}Si_2S_{14}$,[14] $La_6Ga_2GeS_{14}$,[27] and $La_6In_2GeS_{14}$;[27] as well as other sulfides (Li_2ZnGeS_4,[95] Li_2MnGeS_4,[96] $Na_2Hg_3M_2S_8$ (ref. 97)) and pnictides ($RuSi_4P_4$ and $IrSi_3P_3$,[9] $MgSiAs_2$,[98] $Ba_2Si_3P_6$,[99] and $MnSiP_2$ (ref. 100)). A diversity in the nature, content, and oxidation state of transition metal, and ability to modify unit cell volume by tuning RE, Tt, and chalcogen provides ample opportunities for properties tuning.

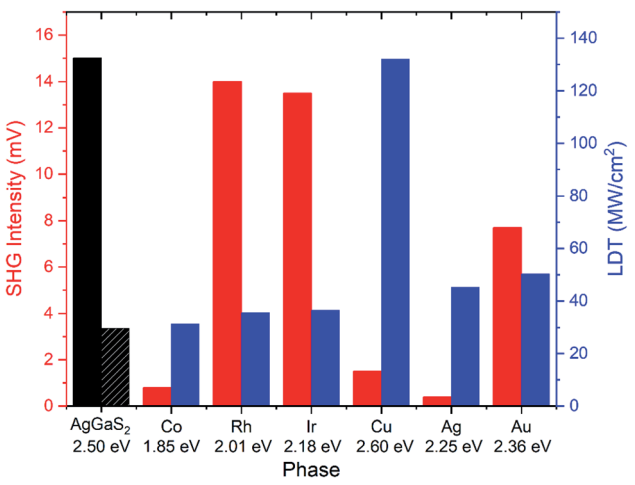

Fig. 8 Second harmonic generation (SHG-red) and laser damage threshold (LDT-blue) data for $La_6(TM)_xSi_2S_{14}$ (red and blue) and $AgGaS_2$ standard (black). TM = Co (x = 1.0); Rh and Ir (x = 0.67); Cu, Ag, and Au (x = 2.0). Particle size = 38.5–54 microns. Corresponding bandgaps (eV) are given below.

Magnetic properties. For the non-magnetic RE = La, magnetic properties are defined by the transition metal. The magnetic susceptibility data for $La_6V_{0.77}Si_2S_{14}$ shows paramagnetic behavior (Fig. 9 and S9†), expected for open-shell configurations including V^{3+} and potential mixed $V^{2+/3+}$ oxidation states. However, low concentration of V ions in the compound makes verification of the valence configuration by Curie–Weiss fit challenging. On the other hand, the data for $La_6Ir_{0.67}Si_2S_{14}$ shows diamagnetic behavior, suggesting a low-spin 3+ oxidation state for Ir (d^6). A weak paramagnetic signal responsible for the upturn in $\chi(T)$ below 50 K is, likely, extrinsic to the $La_6Ir_{0.67}Si_2S_{14}$ compound. The isothermal field dependence of the magnetization at 2 K (Fig. S9†) further shows paramagnetic behavior for the V analogue and diamagnetic for the Ir one. AC susceptibility measurements did not detect any superconductivity in the studied compounds. Replacing La with magnetic rare-earth metal resulted in diverse magnetic properties due to the presence of two magnetic sublattices, RE and

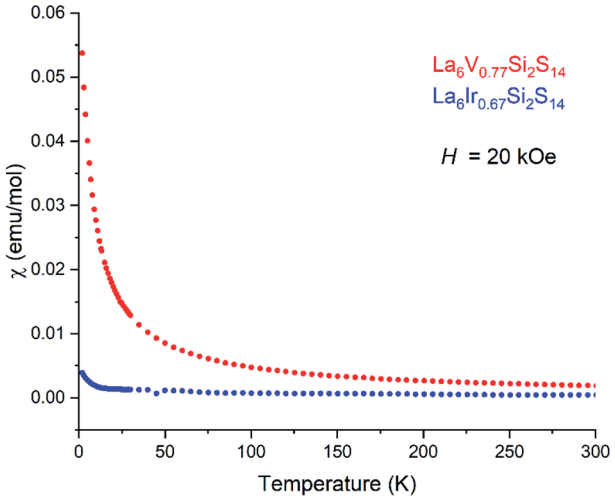

Fig. 9 Temperature-dependent magnetic susceptibility data for $La_6Ir_{0.67}Si_2S_{14}$ (blue) and $La_6V_{0.77}Si_2S_{14}$ (red), collected at an applied field of 20 kOe between 2 and 300 K.

TM. Detailed analyses of the complex magnetic behavior of Pr, Sm, Gd, Tb, Dy, Ho, and Er compounds will be reported in due course.

Conclusions

In this work we have demonstrated a facile method to synthesize multimetallic sulfides apart from traditional synthesis from elements or binary chalcogenides. The developed synthetic method of using precursors with atomically-mixed refractory components produces a range of known and new $RE_6(TM)_x(Tt)_2S_{14}$ phases crystallizing in the polar and chiral $P6_3$ space group. This method is especially useful for underexplored analogues with Tt = Si. Our synthetic method allows for the substantial expansion of the $RE_6(TM)_x(Tt)_2S_{14}$ family to almost the entire transition metal block, providing a large family of semiconductors with tunable bandgaps and electronic configurations. In many cases, single-phase products were obtained without any extensive optimization of the synthetic conditions. Moreover, we have demonstrated the ability to grow large single crystals of certain systems where phase-pure samples are not available.

Together with the previous results in the synthesis of phosphides and arsenides, this method of atomic mixing of refractory components seems to be applicable for synthesis of complex multinary compounds containing volatile and reactive components, such as pnictogens or chalcogens. This method has potential to be used for the synthesis of solid solutions and high-entropy pnictides and chalcogenides where the proper mixing of multiple metals is a prerequisite. The brittleness and composition uniformity of the arc-melted precursor pose certain limitations for the proposed synthetic method. However, these limitations can be bypassed by using mixtures of individual silicides, as exemplified with the V-, Zr-, and Hf-containing $RE_6(TM)_x(Tt)_2S_{14}$.

Funding sources

G. A. is grateful to the Ames Laboratory Spedding Postdoctoral Fellowship for financial support. L. H. and H. W. H. acknowledged the support by the U.S. Department of Energy Office of Science, Science Undergraduate Laboratory Internships (SULI). This work was supported by the Ames Laboratory's Laboratory Directed Research and Development (LDRD) program (G. A., N. W. H., G. V, S. J. L., K. K.). Solid-state NMR work (F. A. P. and A. P.) and magnetic measurements (Y. M.) were supported by the U.S. Department of Energy (DOE), Office of Science, Basic Energy Sciences, Materials Science and Engineering Division. The Ames Laboratory is operated for the U.S. DOE by Iowa State University under contract #DE-AC02-07CH11358. Use of the Advanced Photon Source at Argonne National Laboratory was supported by the U. S. Department of Energy, Office of Science, Office of Basic Energy Sciences, under Contract No. DE-AC02-06CH11357.

Data availability

Data are available per request from authors.

Author contributions

The manuscript was written through contributions of all authors.

Conflicts of interest

Authors declare no conflict of interests.

Acknowledgements

We thank Prof. V. Pecharsky (ISU and Ames Laboratory) for access to the arc-melting setup and Professor Javier Vela (ISU) for the use of the diffuse-reflectance setup. L. P. H. would like to thank Dr A. Pathak (SUNY Buffalo State) for arc-melting training and encouragement to apply to SULI.

References

1 K. Kovnir, Predictive Synthesis, *Chem. Mater.*, 2021, **33**(13), 4835–4841, DOI: 10.1021/acs.chemmater.1c01484.
2 M. G. Kanatzidis, R. Pöttgen and W. Jeitschko, The Metal Flux: A Preparative Tool for the Exploration of Intermetallic Compounds, *Angew. Chem., Int. Ed.*, 2005, **44**(43), 6996–7023, DOI: 10.1002/anie.200462170.
3 P. C. Canfield, New Materials Physics, *Rep. Prog. Phys.*, 2020, **83**(1), 016501, DOI: 10.1088/1361-6633/ab514b.
4 J. Wang, P. Yox and K. Kovnir, Flux Growth of Phosphide and Arsenide Crystals, *Front. Chem.*, 2020, **8**, 186, DOI: 10.3389/fchem.2020.00186.
5 V. V. Klepov, C. A. Juillerat, K. A. Pace, G. Morrison and H.-C. zur Loye, "Soft" Alkali Bromide and Iodide Fluxes for Crystal Growth, *Front. Chem.*, 2020, **8**, 518, DOI: 10.3389/fchem.2020.00518.

6 G. Akopov, J. Mark, G. Viswanathan, S. J. Lee, B. C. McBride, J. Won, F. A. Perras, A. L. Paterson, B. Yuan, S. Sen, A. N. Adeyemi, F. Zhang, C.-Z. Wang, K.-M. Ho, G. J. Miller and K. Kovnir, Third Time's the Charm: Intricate Non-Centrosymmetric Polymorphism in $LnSiP_3$ (Ln = La and Ce) Induced by Distortions of Phosphorus Square Layers, *Dalton Trans.*, 2021, **50**(19), 6463–6476, DOI: 10.1039/D1DT00845E.

7 G. Akopov, G. Viswanathan and K. Kovnir, Synthesis, Crystal and Electronic Structure of La_2SiP_4, *Z. Anorg. Allg. Chem.*, 2021, **647**(2–3), 91–97, DOI: 10.1002/zaac.202000378.

8 S. J. Lee, J. Won, L. Wang, D. Jing, C. P. Harmer, J. Mark, G. Akopov and K. Kovnir, New Noncentrosymmetric Tetrel Pnictides Composed of Square-Planar Gold(I) with Peculiar Bonding, *Chem. - Eur. J.*, 2021, **27**(26), 7383–7390, DOI: 10.1002/chem.202005312.

9 S. Lee, S. L. Carnahan, G. Akopov, P. Yox, L. Wang, A. J. Rossini, K. Wu and K. Kovnir, Noncentrosymmetric Tetrel Pnictides $RuSi_4P_4$ and $IrSi_3P_3$: Nonlinear Optical Materials with Outstanding Laser Damage Threshold, *Adv. Funct. Mater.*, 2021, **31**(16), 2010293, DOI: 10.1002/adfm.202010293.

10 S.-P. Guo, G.-C. Guo, M.-S. Wang, J.-P. Zou, G. Xu, G.-J. Wang, X.-F. Long and J.-S. Huang, A Series of New Infrared NLO Semiconductors, $ZnY_6Si_2S_{14}$, $Al_xDy_3(Si_yAl_{1-y})S_7$, and $Al_{0.33}Sm_3SiS_7$, *Inorg. Chem.*, 2009, **48**(15), 7059–7065, DOI: 10.1021/ic802443n.

11 G. Collin, J. Étienne and P. Laruelle, Composés hexagonaux $L_6B_2C_2X_{14}$ lacunaires ordonnés, *Bull. Soc. Fr. Mineral. Cristallogr.*, 1973, **96**(1), 12–17, DOI: 10.3406/bulmi.1973.6770.

12 N. Zhen, L. Nian, G. Li, K. Wu and S. Pan, A High Laser Damage Threshold and a Good Second-Harmonic Generation Response in a New Infrared NLO Material: $LiSm_3SiS_7$, *Crystals*, 2016, **6**(10), 121, DOI: 10.3390/cryst6100121.

13 Y.-F. Shi, Y. Chen, M.-C. Chen, L.-M. Wu, H. Lin, L.-J. Zhou and L. Chen, Strongest Second Harmonic Generation in the Polar R_3MTQ_7 Family: Atomic Distribution Induced Nonlinear Optical Cooperation, *Chem. Mater.*, 2015, **27**(5), 1876–1884, DOI: 10.1021/acs.chemmater.5b00177.

14 H.-J. Zhao, Syntheses, Crystal Structures, and NLO Properties of the Quaternary Sulfides $RE_3Sb_{0.33}SiS_7$ (RE = La, Pr), *J. Solid State Chem.*, 2015, **227**, 5–9, DOI: 10.1016/j.jssc.2015.03.010.

15 A. Michelet and M. J. Flahaut, Sur les composes du type $La_6MnSi_2S_{14}$, *C. R. Seances Acad. Sci., Ser. C*, 1969, **269**, 1203–1205.

16 G. Collin and P. Laruelle, Structure cristalline de $La_6MnSi_2S_{14}$, *C. R. Seances Acad. Sci., Ser. C*, 1970, **270**, 410–412.

17 L. D. Gulay, I. D. Olekseyuk, M. Wołcyrz and J. Stępień-Damm, The Crystal Structures of R_3CuSnS_7 (R = La–Nd, Sm, Gd–Ho), *Z. Anorg. Allg. Chem.*, 2005, **631**(10), 1919–1923, DOI: 10.1002/zaac.200500153.

18 L. D. Gulay, D. Kaczorowski and A. Pietraszko, Crystal Structure and Magnetic Properties of $Ce_3CuSnSe_7$, *J. Alloys Compd.*, 2005, **403**(1–2), 49–52, DOI: 10.1016/j.jallcom.2005.05.030.

19 M. Daszkiewicz, L. D. Gulay, I. R. Ruda, O. V. Marchuk and A. Pietraszko, La_2SiS_5, *Acta Crystallogr., Sect. E: Struct. Rep. Online*, 2007, **63**(12), i197, DOI: 10.1107/S1600536807058606.

20 M. Daszkiewicz, L. D. Gulay, O. S. Lychmanyuk and A. Pietraszko, Crystal Structure of the $R_3Ag_{1-\delta}SiS_7$ (R = La, Ce, Pr, Nd, Sm, Δ = 0.10–0.23) Compounds, *J. Alloys Compd.*, 2008, **460**(1–2), 201–205, DOI: 10.1016/j.jallcom.2007.05.067.

21 M. Daszkiewicz, Yu. O. Pashynska, O. V. Marchuk, L. D. Gulay and D. Kaczorowski, Crystal Structure and Magnetic Properties of $R_3Fe_{0.5}GeS_7$ (R = Y, La, Ce, Pr, Sm, Gd, Tb, Dy, Ho, Er and Tm), *J. Alloys Compd.*, 2014, **616**, 243–249, DOI: 10.1016/j.jallcom.2014.07.091.

22 M. Daszkiewicz, Yu. O. Pashynska, O. V. Marchuk, L. D. Gulay and D. Kaczorowski, Crystal Structure and Magnetic Properties of $R_3Co_{0.5}GeS_7$ (R = Y, La, Ce, Pr, Nd, Sm, Gd, Tb, Dy, Ho, Er and Tm) and $R_3Ni_{0.5}GeS_7$ (R = Y, Ce, Sm, Gd, Tb, Dy, Ho, Er and Tm), *J. Alloys Compd.*, 2015, **647**, 445–455, DOI: 10.1016/j.jallcom.2015.06.059.

23 H.-Y. Zeng, F.-K. Zheng, G.-C. Guo and J.-S. Huang, Syntheses and Single-Crystal Structures of La_3AgSnS_7, $Ln_3M_xMS_7$ (Ln = La, Ho, Er; M = Ge, Sn; $1/4 \le x \le 1/2$), *J. Alloys Compd.*, 2008, **458**(1–2), 123–129, DOI: 10.1016/j.jallcom.2007.03.136.

24 A. K. Iyer, W. Yin, E. J. Lee, X. Lin and A. Mar, Quaternary Rare-Earth Sulfides $RE_3M_{0.5}GeS_7$ (RE = La–Nd, Sm; M = Co, Ni) and $Y_3Pd_{0.5}SiS_7$, *J. Solid State Chem.*, 2017, **250**, 14–23, DOI: 10.1016/j.jssc.2017.03.009.

25 Y. Zhou, A. K. Iyer, A. O. Oliynyk, M. Heyberger, Y. Lin, Y. Qiu and A. Mar, Quaternary Rare-Earth Sulfides $RE_3M_{0.5}M'S_7$ (M = Zn, Cd; M′ = Si, Ge), *J. Solid State Chem.*, 2019, **278**, 120914, DOI: 10.1016/j.jssc.2019.120914.

26 K. Melnychuk, O. Marchuk, M. Daszkiewicz and L. Gulay, Crystal Structure of Novel $R_3Fe(Co, Ni)_{0.5}SnS_7$ (R = Y, La, Ce, Pr, Nd, Sm, Gd, Tb, Dy and Ho) Compounds, *Struct. Chem.*, 2020, **31**(5), 1945–1957, DOI: 10.1007/s11224-020-01558-0.

27 Y.-F. Shi, Y. Chen, M.-C. Chen, L.-M. Wu, H. Lin, L.-J. Zhou and L. Chen, Strongest Second Harmonic Generation in the Polar R_3MTQ_7Family: Atomic Distribution Induced Nonlinear Optical Cooperation, *Chem. Mater.*, 2015, **27**(5), 1876–1884, DOI: 10.1021/acs.chemmater.5b00177.

28 N. Zhen, L. Nian, G. Li, K. Wu and S. Pan, A High Laser Damage Threshold and a Good Second-Harmonic Generation Response in a New Infrared NLO Material: $LiSm_3SiS_7$, *Crystals*, 2016, **6**(10), 121, DOI: 10.3390/cryst6100121.

29 T. O. Engstrand, K. Wei, R. Baumbach, Y. Xin and S. E. Latturner, Structural Disorder in Intermetallic Boride $Pr_{21}M_{16}Te_6B_{30}$ (M = Mn, Fe): A Transition Metal Cluster and Its Evil Twin, *Inorg. Chem.*, 2020, **59**(4), 2484–2494, DOI: 10.1021/acs.inorgchem.9b03358.

30 A. S. Jayasinghe and S. E. Latturner, Metal Flux Growth of Praseodymium Iron Carbides Featuring FeC_3 Units, *Cryst.*

Growth Des., 2021, **21**(1), 103–111, DOI: 10.1021/acs.cgd.0c00889.

31 X. Ma, B. Chen and S. E. Latturner, Synthesis and Properties of New Multinary Silicides $R_5Mg_5Fe_4Al_xSi_{18-x}$ (R = Gd, Dy, Y, $x \approx 12$) Grown in Mg/Al Flux, *Inorg. Chem.*, 2012, **51**(11), 6089–6095, DOI: 10.1021/ic202735b.

32 P. C. Tucker, J. Nyffeler, B. Chen, A. Ozarowski, R. Stillwell and S. E. Latturner, A Tale of Two Metals: New Cerium Iron Borocarbide Intermetallics Grown from Rare-Earth/Transition Metal Eutectic Fluxes, *J. Am. Chem. Soc.*, 2012, **134**(29), 12138–12148, DOI: 10.1021/ja303370j.

33 J. V. Zaikina, I. Schellenberg, E. M. Benbow, R. Pöttgen and S. E. Latturner, Influence of the La/M Network on Magnetic Properties of Mn $_4$ Tetrahedra in Intermetallic Compounds $La_{21-\delta}Mn_8M_7C_{12}$ (M = Ge, Sn, Sb, Te, Bi), *Chem. Mater.*, 2011, **23**(7), 1768–1778, DOI: 10.1021/cm1028595.

34 K. P. Devlin, N. Kazem, J. V. Zaikina, J. A. Cooley, J. R. Badger, J. C. Fettinger, V. Taufour and S. M. Kauzlarich, $Eu_{11}Zn_4Sn_2As_{12}$: A Ferromagnetic Zintl Semiconductor with a Layered Structure Featuring Extended Zn_4As_6 Sheets and Ethane-like Sn_2As_6 Units, *Chem. Mater.*, 2018, **30**(20), 7067–7076, DOI: 10.1021/acs.chemmater.8b02749.

35 S. Baranets, A. Ovchinnikov and S. Bobev, Complex Structural Disorder in the Zintl Phases $Yb_{10}MnSb_9$ and $Yb_{21}Mn_4Sb_{18}$, *Inorg. Chem.*, 2021, **60**(9), 6702–6711, DOI: 10.1021/acs.inorgchem.1c00519.

36 A. Ovchinnikov, S. Chanakian, A. Zevalkink and S. Bobev, Ultralow Thermal Conductivity and High Thermopower in a New Family of Zintl Antimonides $Ca_{10}MSb_9$ (M = Ga, In, Mn, Zn) with Complex Structures and Heavy Disorder, *Chem. Mater.*, 2021, **33**(9), 3172–3186, DOI: 10.1021/acs.chemmater.0c04940.

37 J. Y. Chan, M. M. Olmstead, S. M. Kauzlarich and D. J. Webb, Structure and Ferromagnetism of the Rare-Earth Zintl Compounds: $Yb_{14}MnSb_{11}$ and $Yb_{14}MnBi_{11}$, *Chem. Mater.*, 1998, **10**(11), 3583–3588, DOI: 10.1021/cm980358i.

38 A. Weiland, K. Wei, G. T. McCandless, J. B. Felder, L. J. Eddy, R. E. Baumbach and J. Y. Chan, Strongly Correlated Electron Behavior in a New Member of the $A_{n+1}B_nX3_{n+1}$ Homologous Series: $Ce_7Co_6Ge_{19}$, *Phys. Rev. Mater.*, 2020, **4**(7), 074408, DOI: 10.1103/PhysRevMaterials.4.074408.

39 A. Weiland, L. J. Eddy, G. T. McCandless, H. Hodovanets, J. Paglione and J. Y. Chan, Refine Intervention: Characterizing Disordered $Yb_{0.5}Co_3Ge_3$, *Cryst. Growth Des.*, 2020, **20**(10), 6715–6721, DOI: 10.1021/acs.cgd.0c00865.

40 K. P. Devlin, J. Zhang, J. C. Fettinger, E. S. Choi, A. K. Hauble, V. Taufour, R. P. Hermann and S. M. Kauzlarich, Deconvoluting the Magnetic Structure of the Commensurately Modulated Quinary Zintl Phase $Eu_{11-x}Sr_xZn_4Sn_2As_{12}$, *Inorg. Chem.*, 2021, **60**(8), 5711–5723.

41 K. P. Devlin, S. Chen, D. Donadio and S. M. Kauzlarich, Solid Solution $Yb_{2-x}Ca_xCdSb_2$: Structure, Thermoelectric Properties, and Quality Factor, *Inorg. Chem.*, 2021, **60**(17), 13596–13606, DOI: 10.1021/acs.inorgchem.1c01906.

42 C. J. Perez, X. Qi, Z. Chen, S. K. Bux, S. Chanakian, B. Li, K. Liu, R. Dhall, K. C. Bustillo and S. M. Kauzlarich, Correction to Improved Power Factor and Mechanical Properties of Composites of $Yb_{14}MgSb_{11}$ with Iron, *ACS Appl. Energy Mater.*, 2020, **3**(3), 2147–2159, DOI: 10.1021/acsaem.9b02168.

43 A. F. May, M.-H. Du, V. R. Cooper and M. A. McGuire, Tuning Magnetic Order in the van Der Waals Metal Fe_5GeTe_2 by Cobalt Substitution, *Phys. Rev. Mater.*, 2020, **4**(7), 074008, DOI: 10.1103/PhysRevMaterials.4.074008.

44 L. D. Sanjeewa, Y. Liu, J. Xing, R. S. Fishman, M. T. K. Kolambage, M. A. McGuire, C. D. McMillen, J. W. Kolis and A. S. Sefat, Stacking Faults and Short-Range Magnetic Correlations in Single Crystal $Y_5Ru_2O_{12}$: A Structure with $Ru^{+4.5}$ One-Dimensional Chains, *Phys. Status Solidi B*, 2021, **258**(2), 2000197, DOI: 10.1002/pssb.202000197.

45 J.-Q. Yan, Y. H. Liu, D. S. Parker, Y. Wu, A. A. Aczel, M. Matsuda, M. A. McGuire and B. C. Sales, A-Type Antiferromagnetic Order in $MnBi_4Te_7$ and $MnBi_6Te_{10}$ Single Crystals, *Phys. Rev. Mater.*, 2020, **4**(5), 054202, DOI: 10.1103/PhysRevMaterials.4.054202.

46 M. S. Likhanov, V. Yu. Verchenko, A. A. Gippius, S. V. Zhurenko, A. V. Tkachev, Z. Wei, E. V. Dikarev, A. N. Kuznetsov and A. V. Shevelkov, Electron-Precise Semiconducting $ReGa_2Ge$: Extending the $IrIn_3$ Structure Type to Group 7 of the Periodic Table, *Inorg. Chem.*, 2020, **59**(17), 12748–12757, DOI: 10.1021/acs.inorgchem.0c01805.

47 V. V. Novikov, K. S. Pilipenko, A. V. Matovnikov, N. V. Mitroshenkov, B. I. Kornev, I. V. Plokhikh, A. S. Tyablikov, E. A. Zvereva, G. Raganyan and A. V. Shevelkov, Low-Temperature Thermodynamic and Magnetic Properties of Clathrate-like Arsenide $Eu_7Cu_{44}As_{23}$, *J. Magn. Magn. Mater.*, 2020, **498**, 166165, DOI: 10.1016/j.jmmm.2019.166165.

48 V. Yu. Verchenko, A. O. Zubtsovskii, Z. Wei, A. A. Tsirlin, E. V. Dikarev and A. V. Shevelkov, From Endohedral Cluster Superconductors to Approximant Phases: Synthesis, Crystal and Electronic Structure, and Physical Properties of $Mo_8Ga_{41-x}Zn_x$ and $Mo_7Ga_{52-x}Zn_x$, *Dalton Trans.*, 2019, **48**(22), 7853–7861, DOI: 10.1039/C8DT04982C.

49 E. Garcia, J. D. Corbett, J. E. Ford and W. J. Vary, Low-Temperature Routes to New Structures for Yttrium, Holmium, Erbium, and Thulium Oxychlorides, *Inorg. Chem.*, 1985, **24**(4), 494–498, DOI: 10.1021/ic00198a013.

50 L.-B. Wu and F.-Q. Huang, Crystal Structure of Trilanthanum Monosilver Monosilicon Heptasulfide, La_3AgSiS_7, *Z. Kristallogr.*, 2005, **220**, 307–308.

51 Z. Tang, A. P. Litvinchuk, H.-G. Lee and A. M. Guloy, Crystal Structure and Vibrational Spectra of a New Viologen Gold(I) Iodide, *Inorg. Chem.*, 1998, **37**(19), 4752–4753, DOI: 10.1021/ic980141q.

52 H. Schmidbaur and A. Schier, Aurophilic Interactions as a Subject of Current Research: An up-Date, *Chem. Soc. Rev.*, 2012, **41**(1), 370–412, DOI: 10.1039/C1CS15182G.

53 K. Ishikawa, T. Isonaga, S. Wakita and Y. Suzuki, Structure and Electrical Properties of Au_2S, *Solid State Ionics*, 1995, **79**, 60–66, DOI: 10.1016/0167-2738(95)00030-A.

54 C. L. Teske, Darstellung und Kristallstruktur von Gold-Barium-Thiostannat(lV), Au_2BaSnS_4, *Z. Anorg. Allg. Chem.*, 1978, **445**(1), 193–201, DOI: 10.1002/zaac.19784450124.

55 K. Chondroudis, J. A. Hanko and M. G. Kanatzidis, Chemistry of Gold in Molten Alkali Metal Polychalcophosphate Fluxes. Synthesis and Characterization of the Low-Dimensional Compounds $A_3AuP_2Se_8$ (A = K, Rb, Cs), $A_2Au_2P_2Se_6$ (A = K, Rb), A_2AuPS_4 (A = K, Rb, Cs), and $AAuP_2S_7$ (A = K, Rb), *Inorg. Chem.*, 1997, **36**, 2623–2632, DOI: 10.1021/ic961376%2B.

56 Y. Yang, Y. Chu, B. Zhang, K. Wu and S. Pan, Unique Unilateral-Chelated Mode-Induced d–P–π Interaction Enhances Second-Harmonic Generation Response in New Ln_3LiMS_7 Family, *Chem. Mater.*, 2021, **33**(11), 4225–4230, DOI: 10.1021/acs.chemmater.1c01133.

57 L. C. Otero-Diaz, K. Hiraga, J. R. Sellar and B. G. Hyde, An Electron Microscope Examination of Scandium Sesquisulphide, Sc_2S_3, and Its Mode of Disordering in the Electron Beam, *Acta Crystallogr., Sect. B: Struct. Sci.*, 1984, **40**(4), 355–359, DOI: 10.1107/S0108768184002299.

58 H. Onken, K. Vierheilig and H. Hahn, Uber Silicid- und Germanidchalkogenide des Zirkons und Hafniums, *Z. Anorg. Allg. Chem.*, 1964, **333**(4–6), 267–279, DOI: 10.1002/zaac.19643330414.

59 T. Kusawake, Y. Takahashi and K.-I. Ohshima, Structural Analysis of the Layered Compounds Cu_xTiS_2, *Mol. Cryst. Liq. Cryst. Sci. Technol., Sect. A*, 2000, **341**(2), 93–98, DOI: 10.1080/10587250008026123.

60 E. Parthé, E. Hohnke and F. Hulliger, A New Structure Type with Octahedron Pairs for Rh_2S_3, Rh_2Se_3 and Ir_2S_3, *Acta Crystallogr.*, 1967, **23**(5), 832–840, DOI: 10.1107/S0365110X67003767.

61 F. K. McTaggart and A. D. Wadsley, The Sulfides, Selenides, and Tellurides of Titanium, Zirconium, Hafnium, and Thorium, *Aust. J. Chem.*, 1958, **11**, 445–457.

62 F. Hulliger, New Compounds with Cobaltite Structure, *Nature*, 1963, **198**, 382–383, DOI: 10.1038/198382b0.

63 S. Nakhal, M. Lerch, J. Koopman, M. M. Islam and T. Bredow, Crystal Structure of 3R-$LiTiS_2$ and Its Stability Compared to Other Polymorphs: Crystal Structure of 3R-$LiTiS_2$, *Z. Anorg. Allg. Chem.*, 2013, **639**(15), 2822–2825, DOI: 10.1002/zaac.201300330.

64 K. Kim, Preparation and Properties of $Co_{9-x}M_xS_8$ (M = Ni, Rh, Ru, and Fe), *Bull. Korean Chem. Soc.*, 1986, **7**, 102–105.

65 P. V. Nutsubidze, V. I. Chechernikov, N. T. Kuznetsov, V. K. Slovyanskikh and N. V. Gracheva, Magnetic Properties of Mixed Sulfides of Uranium and Group-IVA Elements, *Inorg. Mater.*, 1984, **20**(2), 291–292.

66 H. P. B. Rimmington and A. A. Balchin, Crystal Data for Layer Compounds in the Series HfS_xSe_{2-x}), *J. Mater. Sci.*, 1974, **9**, 343–345, DOI: 10.1007/BF00550964.

67 D. Johrendt, Crystal and Electronic Structure of the Tetrahedral V_4 Cluster Compounds GeV_4Q_8 (Q = S, Se), *Z. Anorg. Allg. Chem.*, 1998, **624**(6), 952–958.

68 S. Furuseth, L. Brattas and A. Kjekshus, On the Crystal Structures of TiS_3, ZrS_3, $ZrSe_3$, $ZrTe_3$, HfS_3, and $HfSe_3$, *Acta Chem. Scand., Ser. A*, 1975, **29**, 623–631, DOI: 10.3891/acta.chem.scand.29a-0623.

69 D. Bichler, V. Zinth, D. Johrendt, O. Heyer, M. K. Forthaus, T. Lorenz and M. M. Abd-Elmeguid, Structural and Magnetic Phase Transitions of the V_4-Cluster Compound GeV_4S_8, *Phys. Rev. B: Condens. Matter Mater. Phys.*, 2008, **77**(21), 212102, DOI: 10.1103/PhysRevB.77.212102.

70 T. J. A. Popma, C. Haas and B. Van Laar, Spin Structure and Magnetic Anisotropy of Cr_5S_6 and Rhombohedral Cr_2S_3, *J. Phys. Chem. Solids*, 1971, **32**(3), 581–590, DOI: 10.1016/0022-3697(71)90007-2.

71 G. Kliche, Far-Infrared and X-Ray Investigations of the Mixed Platinum Dichalcogenides $PtS_{2-x}Se_x$, $PtSe_{2-x}Te_x$, and $PtS_{2-x}Te_x$, *J. Solid State Chem.*, 1985, **56**, 26–31.

72 D. T. Hodul and A. M. Stacy, The Structure and Electronic Properties of the Solid Solutions $(Zr_xTi_{1-x})_{1+y}S_2$, *J. Solid State Chem.*, 1986, **62**, 328–334.

73 D. Kuishou, H. Cunhen and Z. Qitai, Determination of Daomanite Crystal Structure, *Kexue Tongbao*, 1982, **27**, 62–66.

74 R. D. Shannon, Revised Effective Ionic Radii and Systematic Studies of Interatomic Distances in Halides and Chalcogenides, *Acta Crystallogr., Sect. A: Found. Crystallogr.*, 1976, **32**, 751–767, DOI: 10.1107/S0567739476001551.

75 J. He, Z. Wang, X. Zhang, Y. Cheng, Y. Gong, X. Lai, C. Zheng, J. Lin and F. Huang, Synthesis, Structure, Magnetic and Photoelectric Properties of $Ln_3M_{0.5}M'Se_7$ (Ln = La, Ce, Sm; M = Fe, Mn; M′ = Si, Ge) and $La_3MnGaSe_7$, *RSC Adv.*, 2015, **5**(65), 52629–52635, DOI: 10.1039/C5RA05629B.

76 A. Michelet, G. Perez, J. Etienne and M. Darriet-Duale, Sur Une Nouvelle Famille de Combinaisons Des Terres Rares de Formules Ln_2SiS_5 (Ln = La à Nd) et Ln_2GeS_5 (Ln = La), *C. R. Seances Acad. Sci., Ser. C*, 1970, **271**, 513–515. https://hal.archives-ouvertes.fr/hal-00111168/.

77 Y. Mudryk, D. Paudyal, J. Liu and V. K. Pecharsky, Enhancing Magnetic Functionality with Scandium: Breaking Stereotypes in the Design of Rare Earth Materials, *Chem. Mater.*, 2017, **29**(9), 3962–3970, DOI: 10.1021/acs.chemmater.7b00314.

78 G. Akopov, M. T. Yeung, Z. C. Sobell, C. L. Turner, C.-W. Lin and R. B. Kaner, Superhard Mixed Transition Metal Dodecaborides, *Chem. Mater.*, 2016, **28**(18), 6605–6612, DOI: 10.1021/acs.chemmater.6b02632.

79 G. Akopov, H. Yin, I. Roh, L. E. Pangilinan and R. B. Kaner, Investigation of Hardness of Ternary Borides of the $YCrB_4$,Y_2ReB_6, Y_3ReB_7, and YMo_3B_7 Structural Types, *Chem. Mater.*, 2018, **30**, 6494–6502, DOI: 10.1021/acs.chemmater.8b03008.

80 M. Daszkiewicz, L. D. Gulay, A. Pietraszko and V. Ya. Shemet, Crystal Structures of the $La_3AgSnSe_7$ and

$R_3Ag_{1-\delta}SnS_7$ (R = La, Ce; Δ = 0.18–0.19) Compounds, *J. Solid State Chem.*, 2007, **180**(7), 2053–2060, DOI: 10.1016/j.jssc.2007.05.007.

81 A. Michelet and M. J. Flahaut, Sur de Nouvelles Familles de Composes Formes Par Les Sulfures Des Terres Rares Avec Le Sulfure de Germanium Ou Le Sulfure de Silicium, *C. R. Seances Acad. Sci., Ser. C*, 1969, **268**, 326–329.

82 S. Bjorgvinsdottir, B. J. Walder, A. C. Pinon and L. Emsley, Bulk Nuclear Hyperpolarization of Inorganic Solids by Relay from the Surface, *J. Am. Chem. Soc.*, 2018, **140**, 7946–7951, DOI: 10.1021/jacs.8b03883.

83 S. M. Martin and J. A. Sills, ^{29}Si and ^{27}Al MASS-NMR Studies of $Li_2S + Al_2S3 + SiS_2$ Glasses, *J. Non-Cryst. Solids*, 1991, **135**, 171–181, DOI: 10.1016/0022-3093(91)90417-5.

84 C. J. Pickard and F. Mauri, All-Electron Magnetic Response with Pseudopotentials: NMR Chemical Shifts, *Phys. Rev. B: Condens. Matter Mater. Phys.*, 2001, **63**(24), 245101, DOI: 10.1103/PhysRevB.63.245101.

85 J. R. Yates, C. J. Pickard and F. Mauri, Calculation of NMR Chemical Shifts for Extended Systems Using Ultrasoft Pseudopotentials, *Phys. Rev. B: Condens. Matter Mater. Phys.*, 2007, **76**(2), 024401, DOI: 10.1103/PhysRevB.76.024401.

86 J. Vícha, S. Komorovsky, M. Repisky, R. Marek and M. Straka, Relativistic Spin–Orbit Heavy Atom on the Light Atom NMR Chemical Shifts: General Trends Across the Periodic Table Explained, *J. Chem. Theory Comput.*, 2018, **14**(6), 3025–3039, DOI: 10.1021/acs.jctc.8b00144.

87 D. Massiot, J. Hiet, N. Pellerin, F. Fayon, M. Deschamps, S. Steuernagel and P. J. Grandinetti, Two-Dimensional One Pulse MAS of Half-Integer Quadrupolar Nuclei, *J. Magn. Reson.*, 2006, **181**(2), 310–315, DOI: 10.1016/j.jmr.2006.05.007.

88 A. A. Galeev, N. M. Khasanova, C. Rudowicz, G. S. Shakurov, A. B. Bykov, G. R. Bulka, N. M. Nizamutdinov and V. M. Vinokurov, Multifrequency EPR Study of Cr^{3+} Ions in $LiScGeO_4$, *J. Phys.: Condens. Matter*, 2000, **12**(20), 4465–4473, DOI: 10.1088/0953-8984/12/20/302.

89 P. Lombard, N. Ollier and B. Boizot, EPR Study of Ti^{3+} Ions Formed under Beta Irradiation in Silicate Glasses, *J. Non-Cryst. Solids*, 2011, **357**(7), 1685–1689, DOI: 10.1016/j.jnoncrysol.2010.12.015.

90 V. Laguta, M. Buryi, A. Beitlerova, O. Laguta, K. Nejezchleb and M. Nikl, Vanadium in Yttrium Aluminum Garnet: Charge States and Localization in the Lattice, *Opt. Mater.*, 2019, **91**, 228–234, DOI: 10.1016/j.optmat.2019.03.024.

91 R. H. Borcherts and L. L. Lohr, Optical, EPR, and ENDOR Studies of $CdF_2:V^{3+}$, V^{2+}, *J. Chem. Phys.*, 1969, **50**(12), 5262–5265, DOI: 10.1063/1.1671043.

92 X. Luo, Z. Li, Y. Guo, J. Yao and Y. Wu, Recent Progress on New Infrared Nonlinear Optical Materials with Application Prospect, *J. Solid State Chem.*, 2019, **270**, 674–687, DOI: 10.1016/j.jssc.2018.12.036.

93 Y. Chu, G. Li, X. Su, K. Wu and S. Pan, A Review on the Development of Infrared Nonlinear Optical Materials with Triangular Anionic Groups, *J. Solid State Chem.*, 2019, **271**, 266–272, DOI: 10.1016/j.jssc.2018.10.051.

94 I. Chung and M. G. Kanatzidis, Metal Chalcogenides: A Rich Source of Nonlinear Optical Materials, *Chem. Mater.*, 2014, **26**(1), 849–869, DOI: 10.1021/cm401737s.

95 J.-H. Zhang, D. J. Clark, J. A. Brant, K. A. Rosmus, P. Grima, J. W. Lekse, J. I. Jang and J. A. Aitken, α-Li_2ZnGeS_4: A Wide-Bandgap Diamond-like Semiconductor with Excellent Balance between Laser-Induced Damage Threshold and Second Harmonic Generation Response, *Chem. Mater.*, 2020, **32**(20), 8947–8955, DOI: 10.1021/acs.chemmater.0c02929.

96 J. A. Brant, D. J. Clark, Y. S. Kim, J. I. Jang, A. Weiland and J. A. Aitken, Outstanding Laser Damage Threshold in Li_2MnGeS_4 and Tunable Optical Nonlinearity in Diamond-Like Semiconductors, *Inorg. Chem.*, 2015, **54**(6), 2809–2819, DOI: 10.1021/ic502981r.

97 K. Wu, Z. Yang and S. Pan, $Na_2Hg_3M_2S_8$ (M = Si, Ge, and Sn): New Infrared Nonlinear Optical Materials with Strong Second Harmonic Generation Effects and High Laser-Damage Thresholds, *Chem. Mater.*, 2016, **28**(8), 2795–2801, DOI: 10.1021/acs.chemmater.6b00683.

98 K. E. Woo, J. Wang, K. Wu, K. Lee, J.-A. Dolyniuk, S. Pan and K. Kovnir, Mg–Si–As: An Unexplored System with Promising Nonlinear Optical Properties, *Adv. Funct. Mater.*, 2018, **28**(30), 1801589, DOI: 10.1002/adfm.201801589.

99 J. Mark, J. Wang, K. Wu, J. G. Lo, S. Lee and K. Kovnir, $Ba_2Si_3P_6$: 1D Nonlinear Optical Material with Thermal Barrier Chains, *J. Am. Chem. Soc.*, 2019, **141**(30), 11976–11983, DOI: 10.1021/jacs.9b04653.

100 T. Yu, S. Wang, X. Zhang, C. Li, J. Qiao, N. Jia, B. Han, S.-Q. Xia and X. Tao, $MnSiP_2$: A New Mid-IR Ternary Phosphide with Strong SHG Effect and Ultrabroad Transparency Range, *Chem. Mater.*, 2019, **31**(6), 2010–2018, DOI: 10.1021/acs.chemmater.8b05015.